

Probing the low-frequency vibrational modes of viruses with Raman scattering—bacteriophage M13 in water

Kong T. Tsen

Eric C. Dykeman

Otto F. Sankey

Arizona State University
Department of Physics
Tempe, Arizona 85287-1504

Shaw-Wei D. Tsen

Johns Hopkins Medical Institutions
Department of Pathology
Baltimore, Maryland 21231

Nien-Tsung Lin

Tzu Chi University
Institute of Microbiology, Immunology
and Molecular Medicine
701, Sec. 3, Chung-Yang Road
Hualien 970, Taiwan

Juliann G. Kiang

Uniformed Services University of the Health Sciences
Armed Forces Radiobiology Research Institute
Bethesda, Maryland 20899

1 Introduction

Viruses are etiologic agents of a multitude of human diseases; however, they can also be made useful for biological and medical research. Recombinant viral vectors, such as vaccinia viruses, have been used as vectors for expressing genes within eukaryotic cells¹ as well as for the delivery of antitumor vaccines.² In addition, bacteriophages such as the M13 phage have been employed as vehicles for the delivery of DNA into bacteria for gene amplification³ and are potential therapeutic agents against bacterial pathogens.⁴ Recently, there has been increased interest in the use of viruses as nanotemplates for the fabrication of nanostructure elements.^{5–9} For example, rod-shaped viruses such as the M13 phage and tobacco mosaic virus (TMV) have been successfully used as biological templates for the synthesis of semiconductor and metallic nanowires.^{5,8,9} Furthermore, genetically modified TMV and M13 phage have been shown to be useful for the self-assembly of nanomaterials into liquid crystals, films, and fibers.^{6,7} It is therefore very likely that genetically programmed viruses will play an important role in developing the next generation of optoelectronic devices and nanoelectronic circuits.

For monitoring the just mentioned self-assembly processes, an *in situ*, nondestructive technique is desirable. Ra-

Abstract. Raman spectroscopy is used to study low-wave-number ($\leq 20 \text{ cm}^{-1}$) acoustic vibrations of the M13 phage. A well-defined Raman line is observed at around 8.5 cm^{-1} . The experimental results are compared with theoretical calculations based on an elastic continuum model and appropriate Raman selection rules derived from a bond polarizability model. The observed Raman mode is shown to belong to one of the Raman-active axial modes of the M13 phage protein coat. It is expected that the detection and characterization of this low-frequency vibrational mode can be used for applications in biomedical nanotechnology such as for monitoring the process of virus functionalization and self-assembly. © 2007 Society of Photo-Optical Instrumentation Engineers. [DOI: 10.1117/1.2718935]

Keywords: lasers in medicine; Raman spectroscopy; Raman effect; laser applications; laser spectroscopy.

Paper 06276R received Oct. 2, 2006; revised manuscript received Nov. 15, 2006; accepted for publication Nov. 20, 2006; published online Mar. 29, 2007.

man spectroscopy has been shown to be a noninvasive technique in material research. To the authors' knowledge, previous studies of viruses using Raman spectroscopy have focused only on the high-frequency (large-wave-number) regions ($\geq 600 \text{ cm}^{-1}$) where the internal virus composition, i.e., localized vibrations of multiply bonded or electron-rich groups in proteins, was studied.^{10,11} In this paper, we report the first observation of low-wave-number ($\leq 20 \text{ cm}^{-1}$) acoustic vibrations of the M13 phage using Raman spectroscopy. The observed vibrations are compared with theoretical calculations based on an elastic continuum model and appropriate Raman intensities and selection rules derived from a continuum limit of the bond polarizability model. The observed Raman mode has been shown to belong to one of the Raman-active axial modes of the M13 phage protein coat. Because of the sensitivity of these frequencies on environments, it is expected that the detection of this low-frequency vibrational mode can be used to monitor and help to control the process of virus functionalization, such as when coating viruses with different materials, attaching viruses to quantum dots and carbon nanotubes, and forming multiple superstructures. Furthermore, knowledge of the vibrational properties of viruses can enhance our understanding of virus structure and help pave the way for the development of novel viral vectors for applications in biology and in medicine.

Address all correspondence to Kong-Thon Tsen, Physics, Arizona State Univ., Tempe, Arizona 85287 United States of America; Tel: 602-965-5206; Fax: 602-965-7954; E-mail: tsen@asu.edu

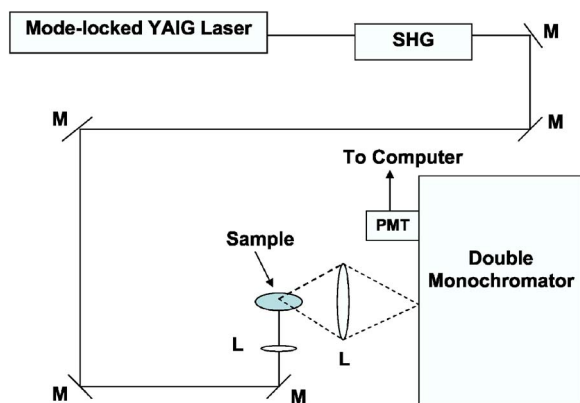


Fig. 1 Experimental setup for our Raman scattering experiments: M; mirrors; L, lens.

2 Samples and Experimental Technique

The M13 phage samples in water solution used in this work were prepared as follows. To propagate the M13 phage, an overnight culture of the host cell, JM101, was diluted 20-fold into 125-mL flasks containing 20 mL of Luria-Bertani (LB) medium. When the culture reached 0.5 of optical density at 550 nm (OD_{550}), the phage was added at a multiplicity of infection of 20 and further grown until stationary phase (ca. 12 h postinfection). Crude phage suspensions were prepared by centrifugation ($10,000 \times g$, 15 min) of the culture to remove the cells and passing the supernatants through a membrane filter (0.45- μm pore size). To concentrate the phage titer, the filtrated supernatant was precipitated by 0.25 M NaCl and 2.5% polyethylene glycol 6000 for 4 h on ice. The pellet collected by centrifugation ($13,500 \times g$ for 15 min at 4°C) was dissolved in 100 μL of distilled water. To determine the phage titer, a double-layer bioassay¹² was performed on a LB agar plate.

To prevent heating of the samples by laser irradiation during the Raman scattering experiments, the second-harmonic generation (SHG) of a cw mode-locked YAIG laser with average power intensity about 10 mW was used as an excitation source.¹³ As depicted in Fig. 1, the laser, which has photon energy of 2.34 eV, was operated at a repetition rate of 76 MHz and has a pulse width of about 70 ps. A scattering geometry of 90 deg was employed. The Raman scattered signal was collected and analyzed by a standard computer-controlled Raman system which included a double spectrometer and a photomultiplier tube (PMT) with associated photon-counting electronics. The spectrometer had a spectral resolution of about 1.0 cm^{-1} . All the data reported here were taken at $T=300 \text{ K}$.

3 Experimental Results and Discussions

A typical Raman scattering spectrum taken for M13 phages at 10^{21} pfu/mL (plaque-forming units per milliliter) and in the spectral range between 2 and 20 cm^{-1} is shown in Fig. 2 (the solid circles). The distinctive feature of the spectrum is a broad structure around 8.5 cm^{-1} sitting on top of a background. To rule out both instrumental artifacts and the possibility of contributions from the DNA within the phages, we repeated the experiments with M13 phages without protein

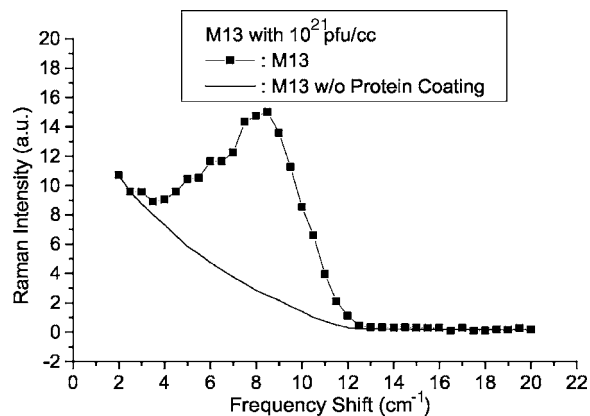


Fig. 2 Raman scattering spectrum of M13 phages in water for a concentration of 10^{21} PFU/mL with (solid circles) and without (solid curve) protein coat. The solid curve represents background signal resulting from the imperfection of rejection of elastic scattering of light by spectrometer.

coats, i.e., with only the single-stranded M13 phage DNA at the same concentration in water. The results are shown as a solid line in Fig. 2. Comparison of the two spectra shows that there is indeed a broad peak at 8.5 cm^{-1} associated with scattering of light from the M13 phage protein coats. The remaining background is due to imperfections in the rejection of elastic light by the spectrometer. Note that based on the Raman setup that we used, we estimate that the lowest frequency vibrational mode that we can confidently detect is about 5 cm^{-1} . The actual low-frequency acoustic vibrational mode signal from the phages is obtained by the subtraction of these two spectra. Figure 3 (connected diamonds) shows the resulting structure after the subtraction. The broad peak has been found to center around 8.5 cm^{-1} . It has a full width at half maximum (FWHM) of about 5.0 cm^{-1} . Since the spectral resolution of our Raman system is about 1.0 cm^{-1} , we conclude that the relatively broad Raman peak observed here very likely results from inhomogeneous broadening.

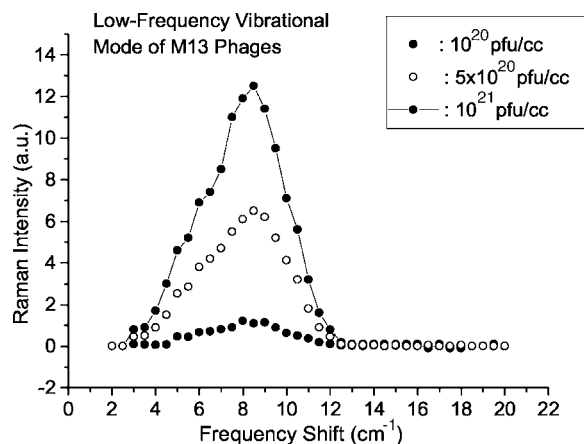


Fig. 3 Raman spectra of the low-frequency vibrational mode of M13 phages for three concentrations in water, as indicated. The Raman intensity has been found to scale with the concentration of the phages, as expected.

Figure 3 shows a comparison of the observed broad structures for the three M13 phage concentrations studied, 1×10^{20} , 5×10^{20} , and 1×10^{21} pfu/mL. The data are properly normalized and therefore are ready for comparison. We find that the integrated areas under the peaks scale very well with the concentration of M13 phages, as expected.

Judging from the SNR of our Raman scattering spectra, we estimate that the lowest concentration of M13 phage that can still be detected using our Raman scattering setup is about 5×10^{19} pfu/mL.

We notice that a likely alternative technique that we can use to compare with our Raman results is the Fourier transform IR (FTIR) absorption technique. In general, FTIR absorption is a technique that is complementary to Raman spectroscopy for the detection of vibrational modes in materials, in particular, if the mode is both Raman active and IR active. However, since water is an extremely strong absorber in the spectral range of our interest, i.e., $\leq 50 \text{ cm}^{-1}$, the detection of vibrational modes of 8.5 cm^{-1} demonstrated in our current Raman work is not feasible by FTIR absorption technique.

To obtain better insight into the character of the observed low-frequency vibrational Raman mode of M13 phages, we performed theoretical calculations in which an elastic continuum model for the M13 viruses is assumed and appropriate Raman selection rules were derived based on a continuum extension of the bond polarizability model.

4 Theoretical Model Calculations

Fonoberov and Balandin investigated low-frequency vibrational modes of viruses used for nanoelectronic self-assembly¹⁴ and phonon confinement effects in hybrid virus-inorganic nanotubes for nanoelectronic applications.¹⁵ In this section, we describe the models used to interpret the Raman spectrum. There are two separate aspects of the problem. They are (1) obtaining the vibrational frequencies (ω) of the modes and their displacement patterns, and (2) from the frequencies and patterns determine their relative Raman scattering intensity. We model the vibrational modes of the M13 phage using elastic wave theory derived from an elastic continuum. The resulting spatial displacement patterns from elastic wave theory (EWT) are then used as input into an amorphous isotropic bond polarizability (AIBP) model to predict the relative Raman intensities of the modes. This analysis is used to determine the characteristics of the vibrational mode at 8.5 cm^{-1} that is being measure in the experiment.

Both ingredients of the analysis, EWT and AIBP, are non-atomistic. These models are valid only for long-wavelength (low-frequency) modes. The low-frequency modes probe global features of the structure and can loosely be described as sound wave resonances within the structure. It is these modes that are of interest in this work. In contrast, more “usual” applications of Raman spectroscopy measure much higher frequencies that are more closely related to individual bonds or bonding groups—here, atomistic approaches would be necessary.

The solutions of EWT are sensitive to the geometry of the virus. The fundamental building unit of the M13 phage is a small peptide chain that has an alpha helix secondary structure, as seen in Fig. 4. These building units self-assemble to create a protein coat of the M13 phage that takes the shape of

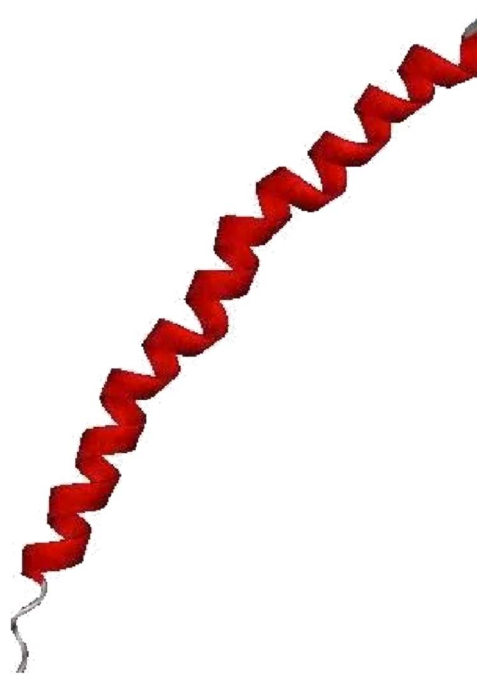


Fig. 4 Single peptide chain building unit of the viral capsid. This unit assembles itself with the helical axis roughly aligned along the central axis of the viral capsid.

a long hollow cylindrical shell. A detailed picture of a section of the assembled protein coat is shown in Fig. 5. The inner hollow part of the protein coat houses the single-stranded DNA (ss-DNA) and water. The viral coat is modeled as a cylindrical shell of inner radius R_a and outer radius R_b .

We first describe EWT. Much of the analysis can be found elsewhere.^{16,17} The fundamental quantity is the displacement pattern \mathbf{u} of the medium, which can be separated into contributions from a scalar (Φ) and vector potential (\mathbf{H}), such that $\mathbf{u} = \nabla\Phi + \nabla \times \mathbf{H}$. These potentials generate separate equations for the transverse and longitudinal elastic waves of the me-

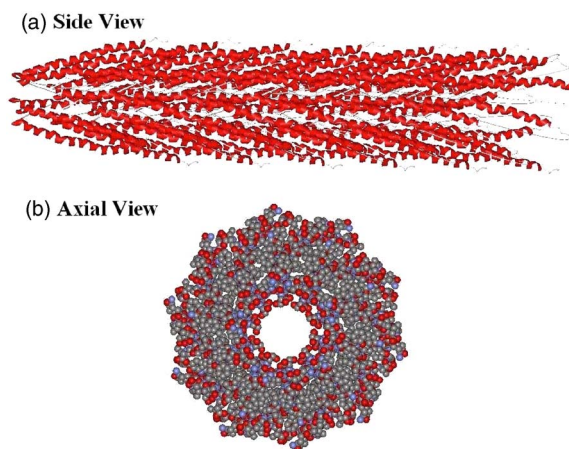


Fig. 5 M13 bacteriophage coat structure composed of single peptide building units: (a) side view of the coat showing the single peptide alpha-helix building units and (b) axial view of the coat representing each atom in the structure as a ball.

dium, namely $\nabla^2\Phi=(1/c_L^2)(\partial^2\Phi/\partial t^2)$ and $\nabla^2\mathbf{H}=(1/c_T^2)\times(\partial^2\mathbf{H}/\partial t^2)$. The solution of these equations in cylindrical coordinates (r, θ, z) involve products of linear combinations of Bessel functions in r [$J_n(\alpha r)$ and $Y_n(\alpha r)$], trigonometric functions $\cos(n\theta)$ or $\sin(n\theta)$ in θ , and e^{ikz} in z . Here α is ω/c_L or ω/c_T , and n is a nonnegative integer ($n=0, 1, 2, \dots$). The tube is assumed to be uniform and infinite along z , giving rise to traveling waves of wave vector \mathbf{k} . The boundary condition on the solutions is that the net radial force vanishes at the inner and outer radii of the tube. This produces a 6×6 determinant, which is required to vanish at the allowed frequencies ω . The corresponding nonzero eigenvector determines the precise linear combination of Bessel functions that comprise the mode pattern at the frequency ω . Full details can be found in Refs. 16 and 18. The solutions to EWT are completely determined by four parameters— c_T , c_L , R_a , and R_b .

The AIBP model uses the displacement pattern of the mode determined from EWT and predicts the mode's relative Raman intensity. We make the usual approximation that the very long wavelength of light only probes the $k=0$ modes. The incident laser light polarizes the material, and the resulting time dependent charge polarization radiates like an antenna. The polarization due to the laser electric field is $\mathbf{p} = \alpha\mathbf{E}$, where α is the polarizability tensor. The polarizability has two contributions. The first is a static component and the second is modulated by the vibrational frequency ω due to perturbation by the oscillation. Thus, the polarization is, $\alpha = \alpha_0 + \Delta\alpha$, where $\Delta\alpha$ is the modulation produced by the vibration. The AIBP model makes two major assumptions. The first is that the polarization can be obtained by summing up the polarization of individual bonds within the material. This assumption has been used in several applications involving crystals and molecules and has been shown to produce good results. Its genesis is the bond-polarizability (BP) model of Go et al.,¹⁹ Snoke and Cardona,²⁰ Dong and Sankey,²¹ and Guha et al.²² and is widely used. Each bond is assumed to have polarizability α_{\parallel} (parallel to the bond), and α_{\perp} (perpendicular to the bond). Changes in the polarizability due to changes in the bond length Δd from a vibrational distortion are described by polarizability derivatives $\alpha' = (d\alpha)/[d(\Delta d)]$. These parameters modulate the components of the parallel and perpendicular components of the BP as $\alpha'_{\parallel}\Delta d$ and $\alpha'_{\perp}\Delta d$, respectively, where Δd varies harmonically. The second major assumption has two subcomponents. Both take the view that over longer length scales the folding and coiling behavior of protein components of the virus can be averaged over as if it were an amorphous isotropic material. The first subcomponent is then that the microscopic chemical identity of each bond is replaced by an average bond. Thus, the variety of BP derivatives is replaced by a single set (\parallel and \perp) of BP derivatives of bond length d . The second subcomponent concerns the direction of the bonds making up the virus. We average the BP tensor over all directions as if the material was truly amorphous.

Clearly the goal of the approximations used is to treat the material as if it were a continuum, thus removing the atomistic dependence from the problem. The final result¹⁸ for the polarization using the AIBP model is in terms of the strain tensor $u_{ij} = \frac{1}{2}(\partial u_i/\partial x_j + \partial u_j/\partial x_i)$ and is given by $\Delta\alpha = \alpha_S u_S$

Table 1 Parameters used for the geometry, elastic wave theory, and the amorphous isotropic bond-polarizability model.

Inner Radius R_a (nm)	Outer Radius R_b (nm)	Longitudinal Sound Speed c_L (m/s)	Transverse Sound Speed c_T (m/s)	Ratio of Polarizabilities α_C/α_S
1.9	3.4	1817	915	0.5

$+ \alpha_C \text{Tr}(\mathbf{u})\mathbf{I}$. Here s and c refer to shear and compressional components, Tr is the trace, $\alpha_S = (2/5)\{[d(\alpha'_{\parallel} - \alpha'_{\perp})/3] + (\alpha_{\parallel} - \alpha_{\perp})\}$, $\alpha_C = \frac{d}{5}(\alpha'_{\parallel} + 2\alpha'_{\perp})$, \mathbf{I} is the identity (unit) tensor, and \mathbf{u}_S is the traceless shear component of the strain tensor, $\mathbf{u}_S = \mathbf{u} - (1/3)\text{Tr}(\mathbf{u})\mathbf{I}$. These relations yield an expression for the Raman intensity for 90-deg scattering of¹⁸ $I = I_0\{13[\text{Tr}(\Delta\chi)^2] - [\text{Tr}(\Delta\chi)]^2\}$, where $\Delta\chi$ is the average susceptibility over the volume of the virus, $\Delta\chi = \int \Delta\alpha d^3r$. The intensity factor I_0 is an overall intensity factor that depends on many things, including the laser intensity. We compute only relative intensities so that it drops out of the analysis. The only nonvanishing contributions after integration¹⁸ are those modes with $n=0, 1$, and 2 in $\cos(n\theta)$ or $\sin(n\theta)$. The Raman intensities for different n values scale with the parameters α_C and α_S as $\alpha_C^2(1/3 + 2\alpha_C/\alpha_S)^2$, α_S^2 and α_S^2 for n equaling 0, 1, and 2, respectively. Absorbing α_S^2 into I_0 for all cases, the results depend only on the ratio α_C/α_S . This reduces the number of parameters from two to one. And then only the relative intensity for the $n=0$ modes depends on this single parameter.

We now summarize the parameters appearing in the model. The five parameters of the model are R_a and R_b (geometry), c_L and c_T (elasticity theory), and the ratio α_C/α_S (the AIBP model). The parameters we use are listed in Table 1.

The radii R_a and R_b are obtained from the size of the protein building unit (Fig. 4) and averaging the diameter of the assembled capsid structure (Fig. 5) obtained from the x-ray diffraction structure.²³ The longitudinal and transverse sound speeds were obtained from measurements of the lysozyme protein.²⁴ These values were also used by Fonoberov and Balandin^{14,15} and Balandin and Fonoberov²⁵ in their pioneering work on tubular viruses. There is no certain method to determine the AIBP ratio α_C/α_S . We can only make an estimate based on a reasonable extrapolation. We consider an "average" bond within the peptide to be a carbon-carbon bond, and determine the ratio α_C/α_S based on experimental measurements²⁰ of carbon-based materials specifically C_{60} . We use a value for α_C/α_S of approximately 0.5 based on these measurements. It is easy to estimate the effect of changing this parameter since $I(n)$ scale as $[(1/2 + 2x)^2, 1, 1]$ for $n=0$ modes, where $x = \alpha_C/\alpha_S$.

We next describe the Raman-active modes that we obtain from $\omega=0$ to 25 cm^{-1} and their character. Then we compute their Raman intensities, and finally compare with experiment. Table 2 lists the Raman-active modes in this range, their character, n value, Raman intensity, and expected damping.

There are 21 modes (not including degeneracies) in this range, of which 10 are Raman, are labeled from 1 to 10 in ascending order of their frequency. Although the frequencies are low on a scale usually measured in Raman scattering, recall that a frequency of 10 cm^{-1} corresponds to 300 GHz,

Table 2 Predicted Raman-active vibrational modes of M13 phage in the frequency range of 0 to 25 cm^{-1} ; all modes have \mathbf{k} vectors along the axis equal to zero (appropriate to Raman experiments).

Mode Number	Frequency ω (cm^{-1})	Character	n value $\cos(n\theta)$ or $\sin(n\theta)$	Relative Raman Intensity (Max.=1)	Damping	Expected Raman Intensity
1	1.22	radial-torsional	2	7.9×10^{-4}	yes	0.00
2	1.85	axial	1	6.1×10^{-2}	no	6.1×10^{-2}
3	3.29	radial	0	2.4×10^{-2}	yes	0.00
4	6.33	radial-torsional	2	0.42	yes	0.00
5	10.48	axial	1	1.00	no	1.00
6	13.39	radial-torsional	2	0.70	yes	0.00
7	18.77	radial-torsional	2	0.21	yes	0.00
8	20.47	radial	0	0.82	yes	0.00
9	20.49	axial	1	2.1×10^{-2}	no	2.1×10^{-2}
10	23.54	radial-torsional	2	0.44	yes	0.00

or 0.3 THz. The character of the modes is described as a solely axial displacement, or a combination of a radial and or torsional displacement. An axial displacement is similar to the motion of a drumhead in that the motion is up or down along the axis of the tube. Radial displacements have their displacement perpendicular to the axis of the tube, i.e., along the radial direction. Finally, the torsional displacements involve a twisting of the tube along the axis. For $n=0$, only radial and axial displacements are possible, while for $n>0$, the modes are either axial modes or a combination of radial and torsional displacements. The angular dependence of the modes is given by its n value. Only $n=0, 1$, or 2 are Raman active. The degeneracy factor $g(n)$ for modes of $n=0, 1$, and 2 is $g(n)=1, 2$, and 2 , respectively. This factor occurs because for $n>0$, both $\sin(n\theta)$ and $\cos(n\theta)$ are possible, but only $\cos(n\theta)$ exists for $n=0$. These degeneracy factors are incorporated into the Raman intensity factors in Table 2. The intensities are relative and the highest intensity is arbitrarily set to unity.

We see that 10 modes potentially could be measured from Raman scattering in this frequency range. However, the experiment finds a single major peak, perhaps due to a single mode. We believe the origin of a single mode is the result of damping of viral modes by the surrounding solution. The character of the modes gives information on which modes are expected to be damped by water and those that are not. Expected highly damped modes are those that are radial (i.e., radial expansion/compression) modes. These have compressional displacements at the surface that push against the surrounding water—in both the exterior and the interior cavities. In contrast, the axial modes have displacements along the tube and are expected to be largely protected from the solution. Their motion relative to water at the surfaces is shearlike rather than compressional.

We take this qualitative argument concerning damping into account in the expected Raman intensity column of Table 2. The expected Raman intensity is removed to zero if the mode

is expected to be damped. We conclude that there are three modes contributing to the experiment. By far the largest contribution is the single axial mode at 10.5 cm^{-1} . The remaining two modes are about 6% or less of the major mode and are not visible through the noise. The sketch of the 10.5 cm^{-1} mode is shown in Fig. 6. The mode is such that the thickness of the tube is near about one half of the radial wavelength. Since the skin of the tube is composed of α helices, a rough interpretation is that the alpha helix experiences a shear with the outer side moving in opposition to the other. Additionally, the mode has $n=1$, which gives the pattern a “tilted” overall behavior with opposite sides of the tube being 180 deg out of phase.

We now compare with experiment. A plot of the theoretical Raman spectra is shown in Fig. 7, which includes only the axial modes in Table 2. We have broadened it by 5 cm^{-1} to mimic the inhomogeneous broadening seen in experiment. We find a large central peak similar to experiment. The additional two peaks at 1.85 and 20.49 cm^{-1} are washed out due to the inhomogeneous broadening and the relatively small intensities compared with the central peak at 10.5 cm^{-1} . Experimentally,

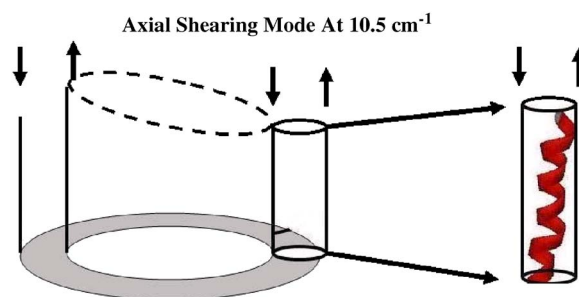


Fig. 6 Displacement pattern for the axial mode with frequency 10.5 cm^{-1} . The resulting displacement of the alpha helical unit block is a shearlike motion.

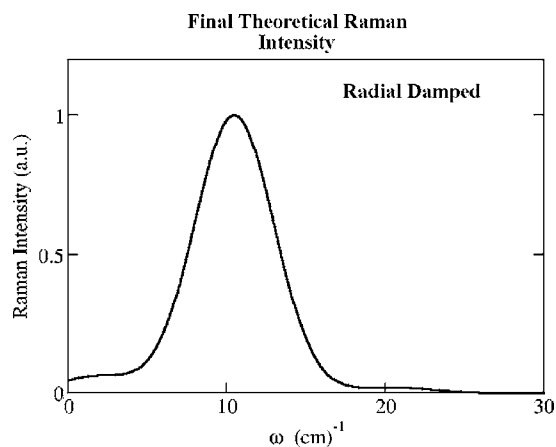


Fig. 7 Theoretical Raman intensity profile taking into account damping of the radial modes due to surrounding water and including a 5 cm^{-1} broadening.

there is one peak at 8.5 cm^{-1} that is in satisfactory agreement with the theoretical spectrum in Fig. 7.

5 Conclusion

Low-frequency vibrational modes of the M13 phage were studied by Raman spectroscopy. The observed vibrational mode at 8.5 cm^{-1} agrees well with theoretical model calculations (predicted at 10.5 cm^{-1}) that are based on an elastic continuum model and a bond polarizability model with Raman selection rules. With the help of theoretical data, we determined that the observed Raman mode corresponds to an axial (drum-head-like) vibrational mode of the M13 phage protein coat that suffers minimal damping in the exterior solvent. Our results suggest that Raman spectroscopy is a feasible, nondestructive technique for probing the process of virus functionalization, such as when coating viruses with different materials, attaching viruses to quantum dots and carbon nanotubes, and forming multiple superstructures. Bacteriophage M13 is one of the simplest paradigms for viral capsids, and the characterization of its low-frequency vibrational modes is a significant step toward the use of vibrational properties in functionalization studies.

Acknowledgments

This work is supported in part by the National Science Foundation under Grant No. DMR-0305147 and by Department of Defense (DOD) RAD II STO C. The opinions or assertions contained herein are the private views of the authors and are not to be construed as official or reflecting the views of the U.S. Department of the Army, the Uniformed Services University of the Health Sciences, or the U.S. Department of Defense.

References

1. B. Moss, "Vaccinia virus: a tool for research and vaccine development," *Science* **252**, 1662–1667 (1991).
2. M. E. G. Bournsnel, E. Rutherford, J. K. Hickling, E. A. Rollinson, A. J. Munro, N. Rolley, C. S. McLean, L. K. Borysiewicz, K. Vouden, and S. C. Inglis, "Construction and characterisation of a recom-

binant vaccinia virus expressing human papillomavirus proteins for immunotherapy of cervical cancer," *Vaccine* **14**(16), 1485–1494 (1996).

3. J. Messing, B. Gronenborn, B. Müller-Hill, and P. H. Hofschneider, "Filamentous coliphage M13 as a cloning vehicle: insertion of a HindIII fragment of the lac regulatory region in M13 replicative form in vitro," *Proc. Natl. Acad. Sci. U.S.A.* **74**, 3642–3646 (1977).
4. C. R. Merrill, B. Biswas, R. Carlton, N. C. Jensen, G. J. Creed, S. Zullo, and S. Adhya, "Long-circulating bacteriophage as antibacterial agents," *Microbiology* **93**(8), 3188–3192 (1996).
5. W. Shenton, T. Douglas, M. Young, G. Stubbs, and S. Mann, "Inorganic-organic nanotube composites from template mineralization of tobacco mosaic virus," *Adv. Mater. (Weinheim, Ger.)* **11**, 253–256 (1999).
6. C. E. Flynn, S. W. Lee, B. R. Peelle, and A. M. Belcher, "Viruses as vehicles for growth, organization and assembly of materials," *Acta Mater.* **51**, 5867–5880 (2003).
7. C. Mao, D. J. Solis, B. D. Reiss, S. D. Kottmann, R. Y. Sweeney, A. Hayhurst, G. Georgiou, B. Iverson, and A. M. Belcher, "Virus-based toolkit for the directed synthesis of magnetic and semiconducting nanowires," *Science* **303**, 213–217 (2004).
8. M. Knez, A. M. Bittner, F. Boes, C. Wege, H. Jeske, E. Maiss, and K. Kern, "Biotemplate of 3-nm nickel and cobalt nanowires," *Nano Lett.* **3**, 1079–1082 (2003).
9. M. Knez, M. Sumser, A. M. Bittner, C. Wege, H. Jeske, T. P. Martin, and K. Kern, "Spatially selective nucleation of metal clusters on the tobacco mosaic viruses," *Adv. Funct. Mater.* **14**, 116–124 (2004).
10. R. Tuma and G. J. Thomas, "Raman spectroscopy of viruses," in *Handbook of Vibrational Spectroscopy*, J. M. Chalmers and P. R. Griffiths, Eds., John Wiley & Sons, Chichester (2002).
11. W. L. Liu, K. Alim, A. A. Balandin, D. M. Mathews, and J. A. Dodds, "Assembly and characterization of hybrid virus-inorganic nanotubes," *Appl. Phys. Lett.* **86**, 253108 (2005).
12. A. Eisenstark, "Bacteriophage techniques," in *Methods in Virology*, Vol. 1. K. Maramorosch and H. Koprowski, Eds., pp. 449–524, Academic Press, New York (1967).
13. K. T. Tsen, Keith R. Wald, T. Ruf, P. Y. Yu, and H. Morkoc, "Electron-optical phonon interactions in ultrathin GaAs-AlAs multiple quantum well structures," *Phys. Rev. Lett.* **67**, 2557–2560 (1991).
14. V. A. Fonoberov and A. A. Balandin, "Low-frequency vibrational modes of viruses used for nanoelectronic self-assembly," *Phys. Status Solidi B Rapid Res. Notes* **12**, R67–R69 (2004).
15. V. A. Fonoberov and A. A. Balandin, "Phonon confinement effects in hybrid virus-inorganic nanotubes for nanoelectronic applications," *Nano Lett.* **5**, 1920–1923 (2005).
16. K. F. Graff, *Wave Motion in Elastic Solids*, Ohio State University Press, New York (1991).
17. L. D. Landau and E. M. Lifshitz, *Theory of Elasticity*, 3rd ed., Pergamon Press, London (1986).
18. E. C. Dykeman, O. F. Sankey, and K. T. Tsen, "Raman intensity predictions for cylindrical viruses," *Phys. Rev. B* (submitted).
19. S. Go, H. Bilz, and M. Cardona, "Bond charge, bond polarizability, and phonon spectra in semiconductors," *Phys. Rev. Lett.* **34**, 580–583 (1975).
20. D. W. Snoke and M. Cardona, "A bond polarizability model for the C_{60} Raman spectrum," *Solid State Commun.* **87**, 121–126 (1993).
21. J. Dong and O. F. Sankey, "Chemical trends of the rattling phonon modes in alloyed germanium clathrates," *J. Appl. Phys.* **87**, 7726–7734 (2000).
22. S. Guha, J. Menendez, J. B. Page, and G. B. Adams, "Empirical bond polarizability model for fullerenes," *Phys. Rev. B* **53**, 13106–13114 (1996).
23. D. A. Marvin, L. C. Welsh, M. F. Symmons, W. R. P. Scott, and S. K. Strauss, "Molecular structure and fd (f1, M13) filamentous bacteriophage refined with respect to X-ray fibre diffraction and solid-state NMR data supports specific models of phage assembly at the bacterial membrane," *J. Mol. Biol.* **355**, 294–309 (2006).
24. M. Tachibana, K. Kojima, R. Ikuyama, Y. Kobayashi, and M. Ataka, "Sound velocity and dynamic elastic constants of lysozyme single crystals," *Chem. Phys. Lett.* **332**, 259–264 (2000).
25. A. A. Balandin and V. A. Fonoberov, "Vibrational modes of nanotemplate viruses," *J. Biomed. Nanotechnol.* **1**, 90–95 (2005).